processes

MDPI

Article

Research on the Control and Performance of Integrated Self-Assembled Micro-Scale Structure of NC-Coated CL-20

Haoran Wang [1], Yibo Hao [1], Lei Su [1], Jingyu Wang [2], Xiaodong Li [2] and Xiaofeng Shi [2,*]

[1] School of Material Science and Engineering, North University of China, Taiyuan 030051, China; haoran.wang.77@gmail.com (H.W.); 2103014121@st.nuc.edu.cn (Y.H.); 2103014204@st.nuc.edu.cn (L.S.)
[2] School of Environmental and Safety Engineering, North University of China, Taiyuan 030051, China; wjingyu@nuc.edu.cn (J.W.); xdlinuc@126.com (X.L.)
* Correspondence: xiaofeng_shi1987@163.com

Abstract: A novel self-assembly approach was employed to produce micro-spherical composite energetic material (EM) comprising 2,4,6,8,10,12-Hexanitro-2,4,6,8,10,12-hexaazaisowurtzitane/nitrocellulose (CL-20/NC) via the spray-drying method, with precise control over parameters such as droplet diameter, ambient temperature, and nozzle injection rate. In this method, NC was utilized as a coating for CL-20 to imbue it with distinct spatial characteristics, thereby mitigating its high sensitivity. Scanning electron microscopy (SEM) and X-ray diffraction (XRD) analyses were conducted to investigate the morphology of the CL-20/NC micro-spheres. Additionally, differential scanning calorimetry (DSC) was employed to study the thermal decomposition kinetics of both CL-20 and CL-20/NC. XRD findings revealed that the crystal structure of CL-20/NC micro-spheres prepared using acetone as the solvent remained unchanged, albeit with noticeable attenuation in diffraction peaks. DSC analysis indicated an increase of 4.87 K and 7.64 K in the thermal explosion critical temperature (T_b) and peak temperature (T_e) of CL-20, respectively. Furthermore, the apparent activation energy was enhanced by 18.65 kJ·mol^{-1}, signifying improved thermal stability. SEM analysis confirmed that the micro-spheres' size ranged from 0.5 μm to 5 μm, displaying a regular spherical shape. Notably, the impact sensitivity (H_{50}) of CL-20/NC tripled compared to raw CL-20.

Keywords: energetic materials; CL-20; NC; spray-drying method; self-assembled; thermal sensitivity

Citation: Wang, H.; Hao, Y.; Su, L.; Wang, J.; Li, X.; Shi, X. Research on the Control and Performance of Integrated Self-Assembled Micro-Scale Structure of NC-Coated CL-20. *Processes* **2024**, *12*, 675. https://doi.org/10.3390/pr12040675

Academic Editor: Christos Argirusis

Received: 17 February 2024
Revised: 19 March 2024
Accepted: 25 March 2024
Published: 27 March 2024

1. Introduction

CL-20, characterized by its caged polycyclic nitramine structure, exhibits higher energy and density in comparison to other monocyclic nitramine explosives such as HMX and RDX, rendering it the preferred material for high-energy explosives and propellants [1]. Nonetheless, CL-20's sensitivity is relatively elevated, thus posing a potential safety hazard when directly applied to propellants [2]. To mitigate this concern, researchers worldwide frequently employ polymers to coat CL-20 with the aim of reducing its sensitivity [3–5]. Among these efforts, Luo et al. [6] synthesized polyurethane-based copolymers for this purpose and observed a significant reduction in CL-20's impact sensitivity post-coating. Similarly, Wang et al. [7] developed estane/CL-20 and EPDM/CL-20 formulations, which effectively decreased mechanical sensitivity and enhanced thermal stability to a certain degree. Despite these advancements, it is noteworthy that the inert nature of the coating materials in all aforementioned studies inevitably results in some energy loss during the explosion process. Additionally, variations in coating materials may impact the overall compatibility and potentially introduce storage and usage limitations for energetic materials. In recent years, the introduction of the Composite Modified Double Base (CMDB) concept has offered a solution to the high sensitivity exhibited by certain energetic materials (EMs) during the formation of composite materials [8]. Researchers have explored utilizing components found in propellants as coating materials to apply a

protective layer onto the surface of nitramine explosives [9]. For instance, Shi et al. [10] employed a spray-drying technique to fabricate RDX/NC composite nitramine particles, resulting in a notable reduction in the mechanical sensitivity of RDX while also enhancing its thermal performance. Nitrocellulose (NC), being an energetic material itself, contributes energy to the composite and enhances its stability.

The spray-drying method presents an efficient and practical approach for the preparation of microscale, and even nanoscale, energetic materials featuring novel structures and properties [11]. This method is executed within a designated spray-drying chamber. Herein, the spray precursor liquid undergoes dispersion into atomized droplets via an atomizing nozzle [12,13]. The rapid evaporation of the solvent occurs upon contact with the heated airflow, yielding the prepared material retrieved through a cyclone separator. In comparison to alternative forming techniques, the spray-drying method offers simplicity, continuity in the process, and relatively low costs. Figure 1 illustrates the schematic diagram of the B-290 mini spray dryer utilized in this study.

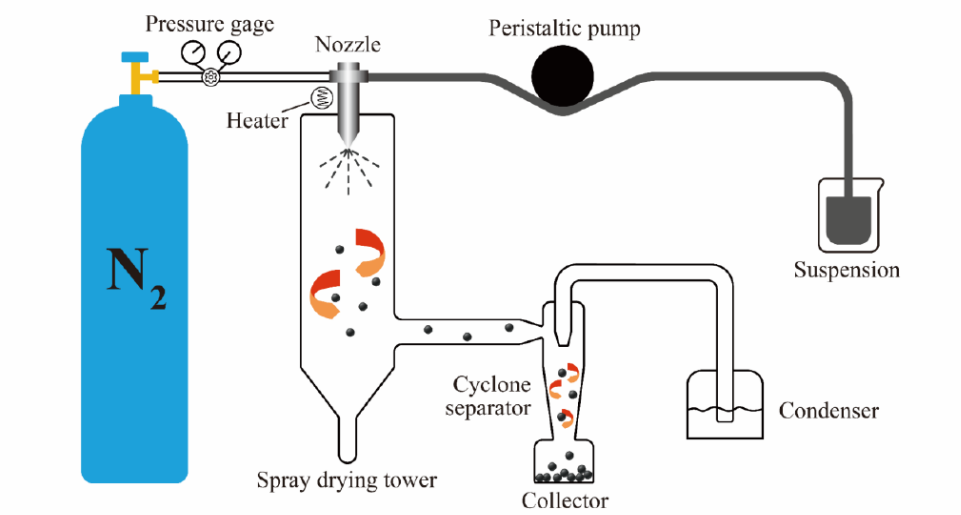

Figure 1. Schematic diagram of the B-290 mini spray dryer.

Spray drying is a method employed to dry a liquid or slurry by dispersing it into a hot gas. This process rapidly vaporizes the liquid, leaving behind a dry powder. Spray drying is recognized as a versatile technique applicable to a diverse range of materials, encompassing food, pharmaceuticals, and chemicals. Numerous studies have demonstrated the synthesis of composite self-assembled energetic materials with unique spatial characteristics through this method. The spray-drying process typically involves several sequential steps: firstly, the liquid is pumped to an atomizer, where it is fragmented into fine droplets. Subsequently, these droplets are introduced into a hot gas chamber. The heat from the gas causes the liquid within the droplets to vaporize, ultimately resulting in the deposition of dry powder particles at the chamber's base, where they are collected. Control over the spray-drying process can be achieved by adjusting various factors, including droplet size, gas temperature, gas flow rate, and solvent concentration within the mixture. This enables the production of energetic material powders tailored to the desired particle size, shape, and dimensional structure. Spray-drying offers several advantages over alternative drying methods: it is characterized by its rapidity, adaptability to a broad spectrum of materials with suitable solvents, and its capacity for continuous production, facilitating the rapid and efficient generation of large quantities of dry powder. This study primarily investigates the influence of nozzle diameter and injection rate on the spray-drying process.

In this study, nitrocellulose (NC) is utilized as both a binder and a coating reinforcement material for CL-20, with modification achieved through the spray-drying method. The resulting coating structure exhibits a favorable degree of sphericity. Furthermore, the thermal decomposition properties of the composites are analyzed. Lastly, the mechanism underlying the thermal decomposition and desensitization is discussed.

2. Materials and Experiment

2.1. Material and Instruments

Material: CL-20 from Gansu Yinguang Chemical Co., Ltd. (Baiyin, China), Nitrocellulose from Sichuan South Nitrocellulose Co., Ltd. (Chengdu, China). Acetone, ethyl acetate, n-heptane, AR, from Tianjin Shentai Chemical Co., Ltd. (Tianjin, China).

Instruments: B-290 Mini Spray Dryer (Buchi Co., Ltd., Lugano, Switzerland). S4800 Cold Field Emission Scanning Electron Microscopy (Hitachi Co., Ltd., Tokyo, Japan), DX-2700 X-ray diffractometer (Dandong Fangyuan Instruments Corporation, Dandong, China), DSC 131 Heat Flow Differential Scanning Calorimeter France Setaram Instruments Ltd., Caluire-et-Cuire, France). Spray refinement device made by the lab.

2.2. The Preparation Methodology

2.2.1. Preparation of Refined CL-20 via Jet Thinning Method ("Solvent/Non-Solvent" Treatment)

CL-20 (20g) was gradually added to 80 mL of ethyl acetate at ambient temperature and pressure, followed by filtration of insoluble materials and impurities subsequent to ultrasonic stirring. Subsequently, 400 mL of n-heptane was measured in a non-solvent container, and the CL-20 solution was transferred into a spray container. Using a spray-drying machine, the CL-20 solution was atomized into droplets via a nozzle, which then descended into the non-solvent n-heptane under gravity. Rapid crystallization of CL-20 particles occurred, resulting in the formation of a white suspension. This suspension was subsequently filtered, washed, subjected to freeze-drying, ultimately yielding CL-20 fine particles with a particle size ranging approximately from 1 to 3 μm.

2.2.2. Preparation of Ultra-Fine CL-20/NC Microsphere via Spray-Drying Method

At ambient temperature, the solution of refined CL-20, which was prepared earlier, and nitrocellulose in a mass ratio of 95:5 is prepared using acetone as the solvent. Subsequently, ultrasonic oscillation is applied for 30 min to ensure complete dissolution and thorough mixing of CL-20 and NC. Following this, the air flux of the spray dryer is adjusted to various injection rates to fully evacuate the air from the apparatus. The temperature is controlled until reaching the default value, after which the precursor solution is pumped into the nozzle. The collection of the product involves isolating the CL-20/NC spherical composite particles from the cyclone separator and hot nitrogen. The preparation roadmap is presented below in Figure 2.

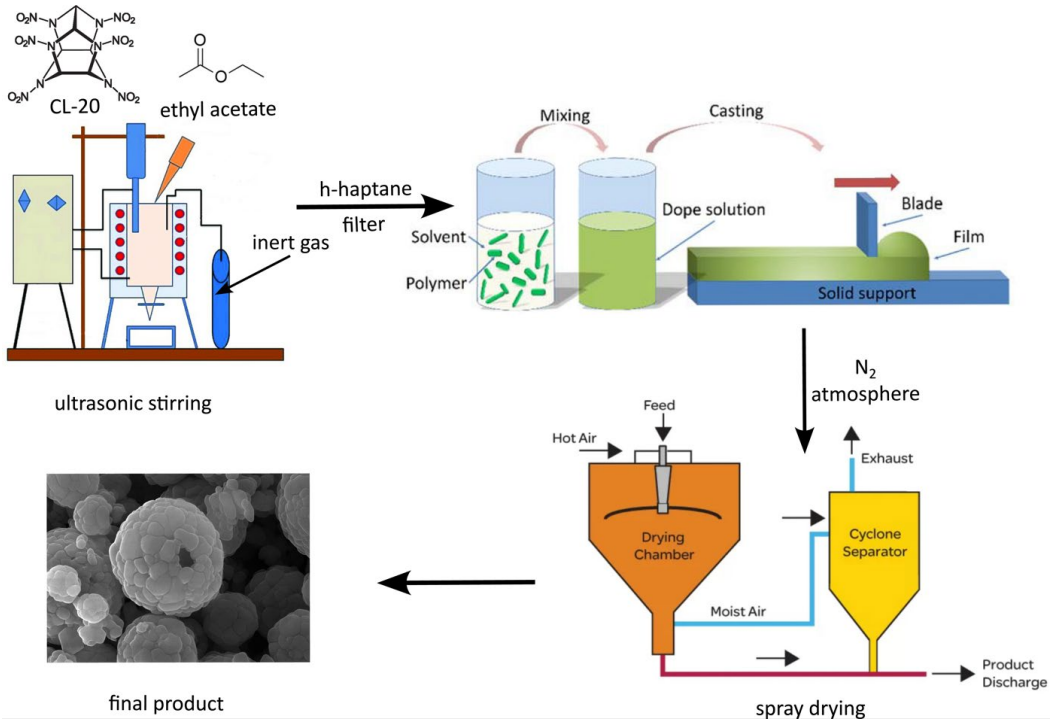

Figure 2. The preparation roadmap of CL-20/NC.

3. Result and Discussion

3.1. Morphology Analysis

3.1.1. SEM Analysis

Figure 3 displays images of CL-20 and CL-20/NC obtained via the spray-drying method. Initially, the particle shape is predominantly spindle-pyramidal, with sizes ranging from 10 to 50 μm. Following the spray-drying process, the shape becomes more uniform, with most particles exhibiting diameters concentrated around 2.0 to 3.3 μm. Notably, some particles even reach smaller diameters, approximately 1 μm, as illustrated in Figure 3b. SEM analysis reveals that the prepared CL-20/NC microspheres exhibit smoother surfaces, indicative of a favorable spheroidization effect.

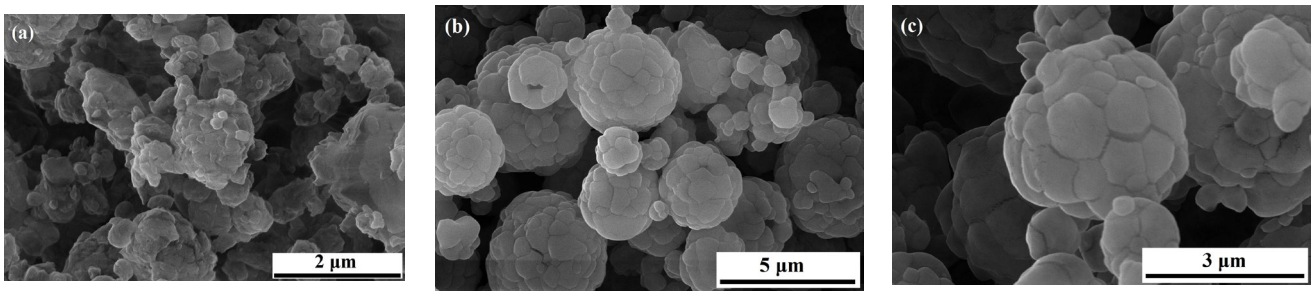

Figure 3. Images of CL-20 and CL-20/NC obtained via the spray-drying method: (**a**) raw CL-20 (10 μm); (**b**) CL-20/NC (8000 magnification); (**c**) CL-20/NC (16,000 magnification).

In Figure 3b, smaller spheres are observed surrounding the larger spheres. This phenomenon can be attributed to the increased supersaturation concentration of the spray precursor solution with rising temperature. The evaporation and crystallization of small droplets atomized through the nozzle in an environment of high supersaturation concentration affect the uniformity of the CL-20 crystal growth process, leading to uneven distribution of fine CL-20 samples. Furthermore, the high temperature accelerates the evaporation of atomized small droplets, causing some CL-20 crystals to dry more rapidly before

they can fully grow, resulting in the formation of tiny particles with higher specific surface area and energy. Additionally, the strong molecular forces facilitate particle aggregation, leading to the formation of larger particles and reducing the specific surface area to maintain stability. To address this issue, reducing the inlet temperature of the liquid feeder of the drying gas used in the spray dryer is proposed as a solution.

Figure 4c illustrates a densely coated layer on the surface of the spheres, indicating effective coating of CL-20 by the NC binders. This observation is further supported by the significant improvement in thermal stability, as indicated by the H_{50} values in Table 4.

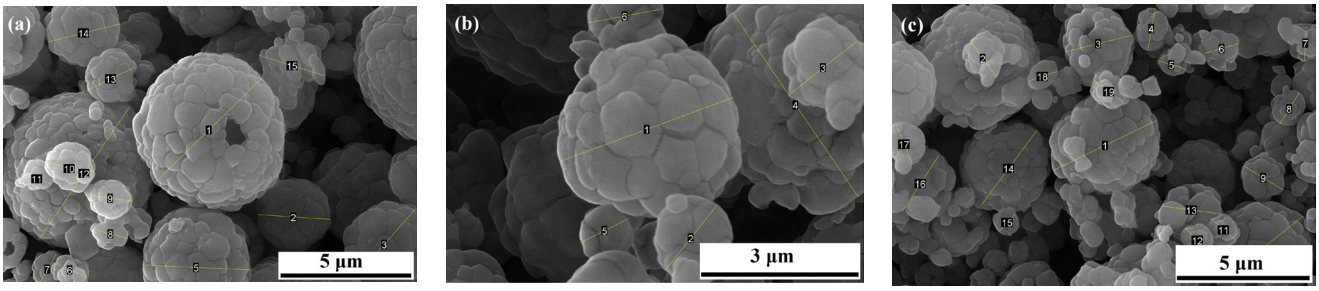

Figure 4. Images of different particle diameters and morphologies with various injection rates and nozzle diameters, respectively: (**a**). 420 L·h^{-1}, 2 mm; (**b**). 340 L·h^{-1}, 1.4 mm; (**c**). 378 L·h^{-1}, 1.4 mm.

Three indicators can be used to assess the overall performance of the product: diameter, coating condition, and morphology. Typically, particles with smaller diameters and favorable morphology, such as hollow holes, exhibit superior performance. Moreover, particles with continuous coating layers demonstrate improved insensitivity. The ideal product, depicted in Figure 4a, features a desirable morphological shape, characterized by both continuous coating layers and hollow holes.

3.1.2. Statistical Analysis

For this study, Class 5 RDX was selected as it represents the finest commercially available powder and serves as a benchmark for comparison with ultrafine spray-dried powders. Figure 4 illustrates the SEM comparison between Class 5 RDX and the final spray-dried RDX samples, highlighting the significant changes in both size and surface appearance resulting from the spray-drying process. Summary data and testing conditions are presented in Table 1.

Table 1. Statistical data of the products.

Sample	Nozzle Diameter/mm	Injection Rate/L·h^{-1}	y_0/μm	x_c/μm	A/μm	FWHM/μm
ingredient			2.46 ± 2.00	2.28 ± 0.80	4.70 ± 8.74	1.70 ± 2.51
1	Ultrasonic nozzle	300	1.17 ± 0.83	1.25 ± 0.41	2.17 ± 1.80	0.45 ± 0.31
2	0.7	300	−0.78 ± 0.07	1.30 ± 0.02	5.77 ± 1.79	1.13 ± 0.20
3	1.4	340	0.33 ± 0.04	1.50 ± 0.94	4.17 ± 6.23	0.91 ± 0.19
4	1.4	378	1.00 ± 0.63	1.45 ± 0.08	5.64 ± 1.55	0.64 ± 0.24
5	2.0	420	0.99 ± 0.33	1.91 ± 0.10	8.10 ± 1.72	1.48 ± 0.46
6	2.0	450	2.29 ± 1.18	2.47 ± 0.72	4.18 ± 2.24	1.45 ± 0.34

It is evident from Figure 5a that the microsphere-like composite energetic material (EM) can only be synthesized using an ultrasonic nozzle. This observation suggests that the nozzle diameter does not exhibit a significant correlation with the fineness of the final product. Additionally, it is observed that both the average diameter and standard deviation increase with the nozzle diameter. Specifically, for the ultrasonic nozzle, the average diameter measures 1.25 μm, with all other results exceeding this value.

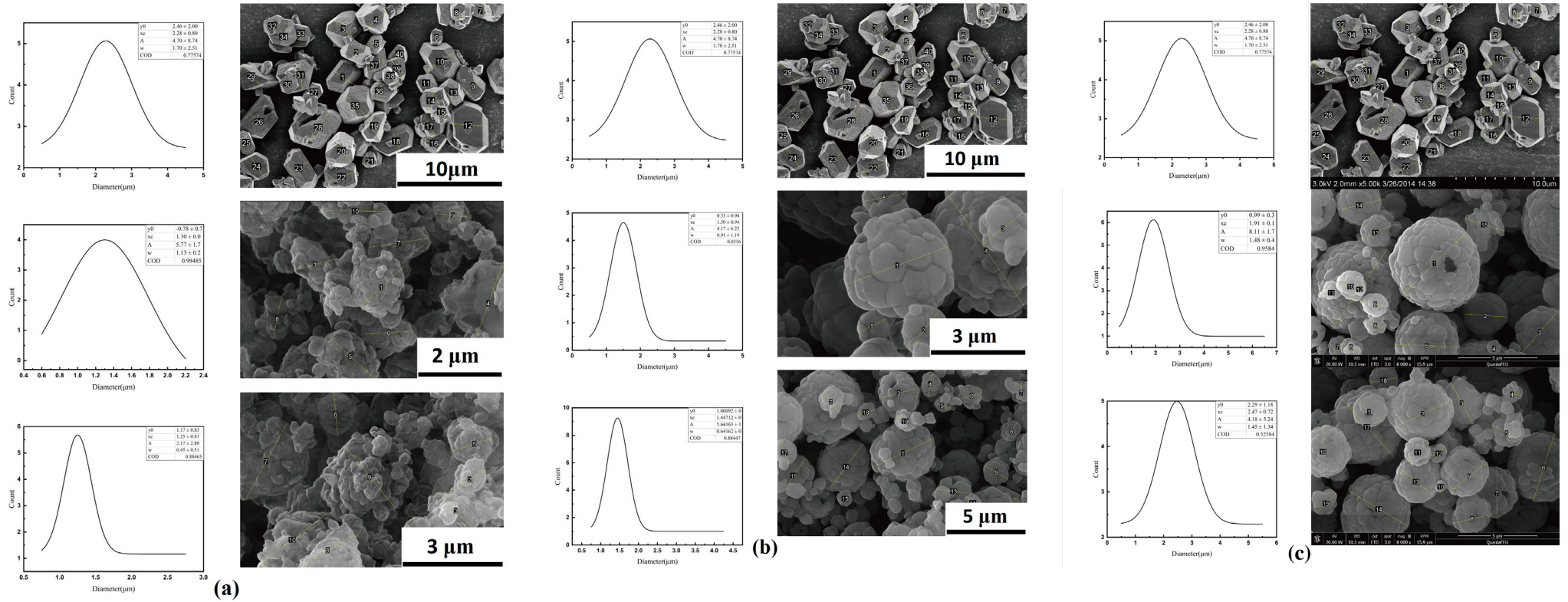

Figure 5. Statistical data and morphology of the products: (**a–c**) the SEM comparison of the initial RDX particles with the products No. 1 and 2, No. 3 and 4, and No. 5 and 6, respectively.

Another crucial factor influencing the overall morphology integrity is the micro-surface texture, primarily attributed to the injection rate of the raw material. The coverage ratio when nitrocellulose (NC) coats the CL-20 particles significantly impacts the final combustion, with the formation of hollow holes enhancing the combustion rate of the composite energetic material (EM). Figure 4 illustrates how the surface morphology varies with different injection rates, ranging from 340 $L \cdot h^{-1}$ to 420 $L \cdot h^{-1}$. It is evident from the experiment that the optimal injection rate is 378 $L \cdot h^{-1}$, as depicted in Figure 4c. This rate facilitates the generation of hollow holes while ensuring nearly full coverage of the surface.

This phenomenon likely occurs because, as the gas flow rate decreases after the material liquid is mixed with the gas, the friction of the droplets ejected from the nozzle decreases, leading to an increase in droplet diameter. Conversely, an increase in gas flux provides greater energy, resulting in smaller droplet diameters. The combined effect of these factors suggests that if the gas flow rate is too high, the residence time of the droplets in the drying cylinder will be shortened, diminishing the drying effect and increasing the diameter of the atomized droplets. Therefore, when acetone and ethyl acetate are used as solvents, the optimal intake flow rate is determined to be 378 $L \cdot h^{-1}$.

3.2. XRD Analysis

The XRD analysis of raw CL-20 and CL-20/NC is depicted in Figure 6, revealing that CL-20 crystallizes in the ε-type structure. Notably, the diffraction peaks' positions of raw CL-20/NC closely align with those of CL-20, suggesting that neither the spray-drying method nor the presence of NC as an adhesive alters CL-20's crystal structure. However, the intensity values differ between the two materials at equivalent diffraction angles. Furthermore, the diffraction peaks of CL-20/NC appear broader compared to those of raw CL-20, as determined by the Scherrer equation [14] (1).

$$D = \frac{0.89\lambda}{\beta \cdot \cos\theta} \quad (1)$$

in which D is the size of crystal CL-20, λ is the wavelength of the incident X-ray, and β is the FWHM value.

The gradual weakening or disappearance of diffraction peaks as particle granularity decreases is a well-known phenomenon. For instance, characteristic peaks of CL-20, typically observed at 12.6°, 13.8°, and 25.8° according to the literature [15], closely align with the data presented in Table 2. Notably, the full width at half maximum (FWHM) values of CL-20/NC are higher than those of CL-20, with some even approximately tripling. While the peak intensity of CL-20/NC at 12.5° surpasses that of CL-20, the overall trend indicates a weakening of diffraction peaks. This weakening can be attributed to the amorphous nature of nitrocellulose, as its coating on CL-20 attenuates the intensity of diffraction peaks. Furthermore, the coating process, which involves a phase change of the adhesive from liquid to solid, accompanied by Van der Waals forces and hydrogen bonding, facilitates the formation of a continuous, uniform coating of polymeric binder on the surface of explosive crystals, thus preserving their crystal form. Consequently, the final product remains in the ε-form crystal structure.

Table 2. Comparison of CL-20/NC and CL-20's characteristic peak data of DSC.

Sample	**Peak Value/a.u.**			**2θ/°**			**FWHM/°**		
Peak	**#1**	**#2**	**#3**	**#1**	**#2**	**#3**	**#1**	**#2**	**#3**
raw CL-20	3346	1053	1575	12.53	13.79	25.75	0.1376	0.1318	0.2201
CL-20/NC	3596	302	1246	13.63	15.55	24.13	0.2262	0.5298	0.3404

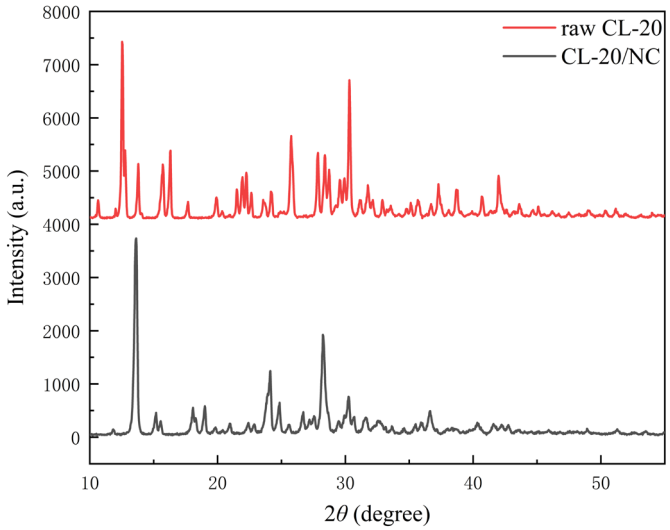

Figure 6. X-ray diffraction of raw CL-20 and CL-20/NC.

3.3. DSC Analysis

The thermal decomposition characteristics of raw CL-20 and CL-20/NC samples, each weighing 0.5 mg, were analyzed using the DSC method under N_2 atmosphere.

According to ICTAC, 4 different heat rate DSC tests were performed to analyze the thermal decomposition characteristics of CL-20 and CL-20/NC. Figure 7a and Figure 7b display the DSC curves of CL-20 and CL-20/NC, respectively. Heating rates (β) of 5 K·min^{-1}, 10 K·min^{-1}, and 15 K·min^{-1} were employed for raw CL-20, whereas for CL-20/NC, heating rates of 5 K·min^{-1}, 10 K·min^{-1}, and 20 K·min^{-1} were used. The decomposition peak temperatures of CL-20/NC were recorded as 238.78 °C, 246.32 °C, 256.61 °C, and 254.04 °C at heating rates of 5 °C·min^{-1}, 10 °C·min^{-1}, 15 °C·min^{-1}, and 20 °C·min^{-1}, respectively. These temperatures are lower compared to the decomposition peak temperatures of raw CL-20, which were measured at 242.61 °C, 250.45 °C, 252.03 °C, and 259.14 °C, representing a difference of 3.83 °C, 4.13 °C, 4.58 °C, and 5.10 °C, respectively.

The thermal decomposition kinetic parameters of the raw material and CL-20/NC were calculated using Kissinger's equation [16] (1) and the thermal explosion critical temperature equation [17] (2), based on the data obtained from the DSC test. The results are presented in Table 2.

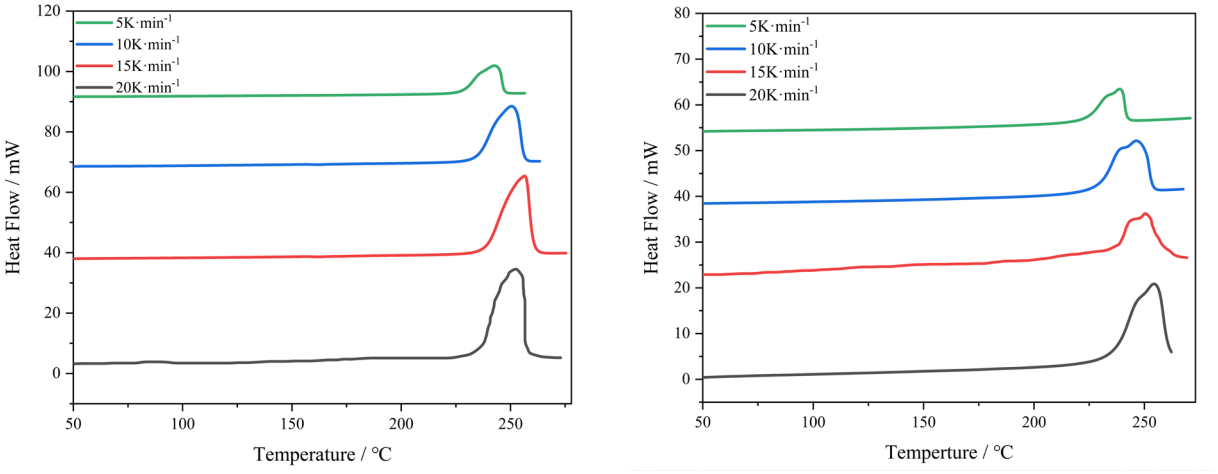

Figure 7. DSC of raw (**a**) CL-20 and (**b**) CL-20/NC.

$$\ln \frac{\beta_i}{T_{pi}^2} = \ln \frac{AR}{E} - \frac{E}{RT_{pi}} \quad (2)$$

$$T_e = T_{pi} - b\beta_i - c\beta_i^2 \quad (3)$$

$$T_b = \frac{E - \sqrt{E^2 - 4RET_e}}{2R} \quad (4)$$

in which, β_i is the heating rate, K·min^{-1}, T_{pi} is the decomposition peak temperature, K. A is the pre-exponential factor, min^{-1}. R = 8.314 J·mol^{-1}·K^{-1}, the molar gas constant. E is the apparent activation energy, J·mol^{-1}. T_e is the peak temperature when the heating rate is zero, K. T_b is the critical temperature of the thermal explosion, K.

Substitute the value of E and T_e obtained by Equation (3) previously into Zhang-Hu-Xie-Li's Critical Temperature of Thermal Explosion [18] (4). The T_b of CL-20 and CL-20/NC can be obtained as shown in Table 3. The fitting curves of CL-20 and CL-20/NC obtained by Kissinger's method are shown in Figure 8, which indicates well fit of the model.

Table 3. Thermal parameters of raw CL-20 and CL-20/NC.

Sample	[1] E/kJ·mol^{-1}	[2] A	[3] T_e/K	[4] T_b/K
raw CL-20	173.25	1.37×10^{17}	523.60	526.72
CL-20/NC	192.01	1.60×10^{19}	528.44	534.53

[1] E is apparent activation energy, J·mol^{-1}; [2] A is pre-exponential factor, min^{-1}; [3] T_e is peak temperature when heating rate is zero, K; [4] T_b is critical temperature of thermal explosion, K.

The apparent activation energy of CL-20/NC is 192.01 kJ·mol^{-1}, which is 18.76 kJ·mol^{-1} more compared to raw CL-20. T_b and T_e also increased by 4.84 K and 7.81 K, respectively. This is maybe because the particle size of refined CL-20 becomes smaller and the specific surface area increases, which enhances the heat transfer performance and accelerates the decomposition and detonation of the explosive.

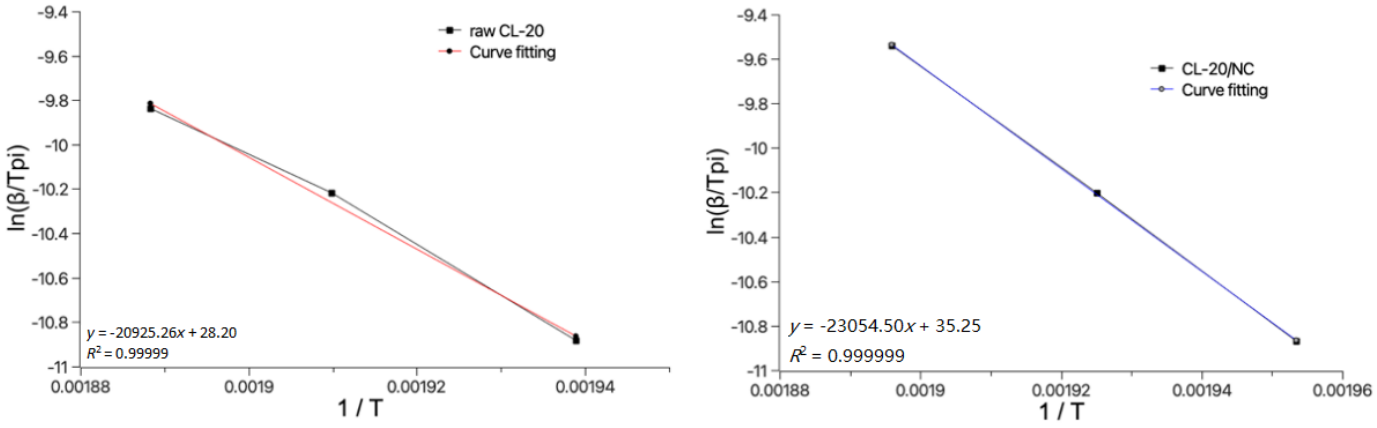

(**a**) (**b**)

Figure 8. Fitting curves of (**a**) CL-20 and (**b**) CL-20/NC obtained by Kissinger's method.

3.4. Impact Sensitivity Study and Detonation Performance

According to the GJB-772A-1997 standard method 601.2 [19], the test was conducted using a Model 12 Drop Weight Tester. The testing conditions are listed below (two repeated experiments were performed): sample mass: 35 ± 1 mg, ambient temperature: 10 °C to 35 °C, dropper weight: 5 ± 0.002 kg, relative humidity ≤ 80%. The test results are presented in Table 4. The impact sensitivity (H_{50}) height of CL-20/NC is 32 cm higher than

that of raw CL-20, representing a 213.33% increase compared to raw CL-20. For comparison, the H_{50} and *VoD* of HMX are 11 cm and 9100 m·s^{-1}, which CL-20/NC is identical to HMX.

Table 4. Results of impact sensitivity for raw CL-20 and CL-20/NC.

Sample	Drop Height (H_{50})/cm	*VoD*/m·s^{-1}
raw CL-20	15	9200
CL-20/NC	47.0	9180
HMX	11	9100

Detonation velocity (*VoD*) serves as an index parameter for explosive output energy [20]. It was observed that the *VoD* of CL-20/NC can reach 9180 m·s^{-1}, nearly equivalent to that of the current military standard explosive octogen (HMX). In conclusion, the CL-20/NC microspheres prepared by the spray-drying method exhibit not only insensitivity to impact but also high detonation performance.

The applications of the Ems are in munitions that are chemically stable enough to withstand various stimuli during storage and transportation and can still explode as intended to defeat their targets. The use of insensitive energetic materials significantly improves the protection of modern nuclear warheads and increases the survivability of conventional munitions in a hustle environment.

4. Mechanism of the Desensitization of the Obtained Composites

In 1952, Bowden et al. [21] systematically elaborated on the concept of "hot spots" while investigating heterogeneous energetic materials: defects such as impurities, voids, and grain boundaries can result in non-uniform internal density within energetic materials. Upon impact, a shock wave propagates through these areas of uneven density, generating localized high-temperature zones known as "hot spots". Additionally, they experimentally determined that the size of hot spot formation ranges from 0.1 to 10 μm, with a brief duration of 10^{-5} to 10^{-3} s [22].

The spray-drying method contributes to the improved performance of CL-20/NC compared to raw CL-20 in several ways: The spray-drying method can produce sub-micron composite particles with a spherical shape, and the size and shape of the particles can significantly influence the combustion and detonation properties of the explosive. It is believed that NC forms hydrogen bonds with CL-20. This results in increased affinity and reduced appearance of hot spots in CL-20/NC composites, which can reduce the impact and friction sensitivities of CL-20 and thus, lower the decomposition peak temperature of CL-20. This means that the explosive can release more energy per unit mass, making it more efficient.

Under external loading, energetic materials undergo stress dissipation and relaxation of defect structures, leading to localized concentration of heat and the formation of nanoscale hot spots. As defects evolve and chemical reactions occur, these hot spots gradually expand into micron-scale regions. Once the hot spot reaches critical conditions, spontaneous growth and expansion occur, ultimately triggering macroscopic ignition and detonation.

In this experiment, CL-20/NC demonstrated superior performance over CL-20 due to several factors. Firstly, the raw material CL-20 possesses relatively large particle size and uneven distribution, with irregular edges on the surface. Upon impact, these raw crystals undergo friction, promoting stress concentration and facilitating the formation and expansion of hot spots. In contrast, the ultra-fine CL-20 particles obtained through spray recrystallization exhibit a smooth, spherical surface, uniform particle size, and increased specific surface area. Consequently, when subjected to mechanical impact, the impact energy is efficiently and evenly distributed among each CL-20 crystal particle [11], reducing the likelihood of hot spot formation. Even if hot spots do occur, they are more prone to

dissipate or fail to reach critical conditions. Consequently, CL-20/NC composites demonstrate enhanced resistance to macroscopic impacts.

5. Conclusions and Expectations

Microspherical CL-20/NC composites were successfully prepared using the spray-drying method, resulting in microspheres ranging in size from 0.5 μm to 5 μm with a regular spherical shape, as confirmed by SEM analysis. XRD analysis was employed to compare the crystal structures. Additionally, the thermal decomposition kinetic parameters and characteristics of the ultrafine CL-20/NC were analyzed using DSC, revealing an enhancement in apparent activation energy by 18.65 $kJ \cdot mol^{-1}$. The CL-20/NC composite demonstrates significant improvements in impact stability and thermal stability, with its impact sensitivity (H_{50}) tripling compared to raw CL-20. In conclusion, CL-20/NC offers several advantages and lays the groundwork for the preparation of subsequent CL-20-based composite explosives.

Researchers are actively involved in customizing CL-20-based materials to suit specific applications, spanning from military munitions and rocket propellants to diverse industrial uses. This tailored approach is vital to ensure that the material fulfills the distinct requirements of each application. Furthermore, significant emphasis is placed on developing CL-20-based materials with long-term stability to mitigate the risk of degradation over time, which is crucial for effective stockpile management. As with any advancing technology, there is an anticipation of cost reduction as production methods improve and become more efficient, thereby expanding the potential applications for cost-effective CL-20-based materials.

Author Contributions: Conceptualization, H.W. and X.S.; methodology and experiment, H.W. and Y.H.; calculation, data analysis and visualization, H.W. and L.S.; validation, Y.H.; formal analysis, H.W. and L.S.; resources, X.S.; writing—original draft preparation, H.W.; writing—review and editing, X.S., J.W. and X.L.; project administration, H.W. and X.S. All authors have read and agreed to the published version of the manuscript.

Funding: This research received no specific grant from any funding agency in the public, commercial, or not-for-profit sectors.

Data Availability Statement: Data are contained within the article.

Conflicts of Interest: The authors declare that they have no known competing financial interests or personal relationships that could have appeared to influence the work reported in this paper.

References

1. Mahnaz, F.; Mostafa-Al-Momin, M.; Rubel, M.; Ferdous, M.; Azam, M.S. Mussel-inspired immobilization of Au on bare and graphene-wrapped Ni nanoparticles toward highly efficient and easily recyclable catalysts. *RSC Adv.* **2019**, *9*, 30358–30369. https://doi.org/10.1039/C9RA05736F.
2. Guo, D.; An, Q.; Goddard, W.A., III; Zybin, S.V.; Huang, F. Compressive Shear Reactive Molecular Dynamics Studies Indicating That Cocrystals of TNT/CL-20 Decrease Sensitivity. *J. Phys. Chem. C* **2014**, *118*, 30202–30208. https://doi.org/10.1021/jp5093527.
3. Greenberg, B.L.; Kalyon, D.M.; Erol, M.; Mezger, M.; Lee, K.; Lusk, S. Analysis of Slurry-Coating Effectiveness of CL-20 Using Grazing Incidence X-ray Diffraction. *J. Energ. Mater.* **2003**, *21*, 185–199.
4. Lee, K.E.; Hatch, R.L.; Braithwaite, P. Method of Making High Performance Explosive Formulations Containing CL-20. U.S. Patent No. 6,217,799, 17 April 2001.
5. Zhigach, A.; Leipunskii, I.O.; Berezkina, N.G.; Pshechenkov, P.A.; Zotova, E.S.; Kudrov, B.V.; Gogulya, M.F.; Brazhnikov, M.A.; Kuskov, M.L. Aluminized nitramine-based nanocomposites: Manufacturing technique and structure study. *Combust. Explos. Shock Waves* **2009**, *45*, 666–677.
6. Yin, Y.; Yunjun, L.; Yongbin, J.; Dumena; Zhen, G.; Chunpeng, C. Study on the Influence of Hard Segment Content of Thermoplastic Polyurethane on the Insensitivity Effect of CL-20. *Chin. J. Energ. Mater.* **2007**, *15*, 395–399.
7. Yu, W.; Wang, J.; Hou, C. Preparation and Characterization of Hexanitrohexaoxaisowurtzitane/Estane Microspheres. *Sci. Technol. Eng.* **2016**, *16*, 192–194. https://doi.org/10.3969/j.issn.1671-1815.2016.09.033.
8. Ye, B.Y.; Wang, J.Y.; An, C.W.; Yu, B.S.; Ji, W.; Li, H.Q. Preparation and Properties of CL-20 Based Composite Energetic Materials. *J. Solid Rocket Tech.* **2017**, *2*, 69–73.

9. Wang, S.-W.; Song, X.-D.; Wu, Z.-K.; Xiao, L.; Zhang, G.-P.; Hu, Y.-B.; Hao, G.-Z.; Jiang, W.; Zhao, F.-Q. Simulation of the plasticizing behavior of composite modified double-base (CMDB) propellant in grooved calendar based on adaptive grid technology. *Def. Technol.* **2021**, *17*, 1954–1966. https://doi.org/10.1016/j.dt.2021.05.008.
10. Shi, X.; Wang, J.; Li, X. Preparation and Properties of RDX-Nitrocellulose Microspheres. *Cent. Eur. J. Energ. Mater.* **2016**, *13*, 871–881.
11. Ma, X.; Li, Y.; Hussain, I.; Shen, R.; Yang, G.; Zhang, K. Core–Shell Structured Nanoenergetic Materials: Preparation and Fundamental Properties. *Adv. Mater.* **2020**, *32*, 2001291. https://doi.org/10.1002/adma.202001291.
12. Qiu, H.; Stepanov, V.; Di Stasio, A.R.; Surapaneni, A.; Lee, W.Y. Investigation of the crystallization of RDX during spray drying. *Powder Technol.* **2015**, *274*, 333–337. https://doi.org/10.1016/j.powtec.2015.01.032.
13. Zhao, X.; Yang, Z.; Qiao, S.; Piao, J.; Li, H. Morphology and properties of CL-20/MTNP cocrystal prepared via facile spray drying. *FirePhysChem* **2022**, *3*, 158–163. https://doi.org/10.1016/j.fpc.2022.10.002.
14. Holzwarth, U.; Gibson, N. The Scherrer equation versus the 'Debye-Scherrer equation'. *Nat. Nanotechnol.* **2011**, *6*, 534. https://doi.org/10.1038/nnano.2011.145.
15. Yuan, B.; Zhang, Y.; Wang, K.-X.; Wang, T.-P.; Li, Y.; Zhu, S.-G.; Zhang, L.; Yi, Z.-X.; Guan, H.; Zhu, C.-G. Tuning the Energetic Performance of CL-20 by Surface Modification Using Tannic Acid and Energetic Coordination Polymers. *ACS Omega* **2022**, *7*, 10469–10475. https://doi.org/10.1021/acsomega.1c07282.
16. Kissinger, H.E. Reaction Kinetics in Differential Thermal Analysis. *Anal. Chem.* **1957**, *29*, 1702–1706. https://doi.org/10.1021/ac60131a045.
17. Xue, L.; Zhao, F.Q.; Hu, R.Z.; Gao, H.X. A Simple Method to Estimate the Critical Temperature of Thermal Explosion for Energetic Materials Using Nonisothermal DSC. *J. Energ. Mater.* **2010**, *28*, 17–34. https://doi.org/10.1080/07370650903124518.
18. Zhang, T.; Hu, R.; Yi, X.; Li, F. The estimation of critical temperatures of thermal explosion for energetic materials using non-isothermal DSC. *Thermochim. Acta* **1994**, *244*, 171–176. https://doi.org/10.1016/0040-6031(94)80216-5.
19. *GJB/772 A-97*; Experimental Methods of Sensitivity and Safety. National Military Standard of China: Beijing, China, 1997. (In Chinese).
20. Li, X.; Han, Z.; Sun, S. Existence of positive solutions of nonlinear fractional q-difference equation with parameter. *Adv. Differ. Equ.* **2013**, *2013*, 260. https://doi.org/10.1186/1687-1847-2013-260.
21. Bowden, F.P.; Yoffe, A.D. *Initiation and Growth of Explosion in Liquids and Solids*; Cambridge University Press: Cambridge, UK, 1985.
22. Field, J.E.; Bourne, N.K.; Palmer, S.J.P.; Walley, M. Hot-spot ignition mechanisms for explosives and propellants. *R. Soc.* **1992**, *339*, 1654. https://doi.org/10.1098/rsta.1992.0034.